Acta Geologica Sinica (English Edition), 2025, 99(6): 1602–1614

Landslide Hazards Identification and Evaluation along the Vakhsh River in Tajikistan based on InSAR Time Series and the MassMov2D Model

SUN Yanqing[1], XU Wenbin[1, *], XIE Lei[1], CHEN Zhidan[1], ZHU Lingjie[1], SUO Zhihui[1] and LIANG Feng[2]

[1] *School of Geosciences and Info-Physics, Central South University, Changsha 410083, China*
[2] *State Key Laboratory of Deep Earth and Mineral Exploration, Chinese Academy of Geological Sciences, Beijing 100094, China*

Abstract: The boundary zones of compressive orogenic belts are particularly susceptible to active landslides due to high topographic relief and intense erosion. The Nurek section of Vakhsh River, located on the western margin of the Pamir orogenic belt, is characterized by complex terrain and severe water erosion. Therefore, the identification and interpretation of potential landslides are significant for regional hazard risk assessment. This study uses Interferometric Synthetic Aperture Radar (InSAR) data and the Small Baseline Subset (SBAS) method to evaluate the potential landslides from October 2017 to December 2023 in this river section, which is prone to frequent landslide occurrences. The results show that six potential landslides were identified, mainly concentrated on the west bank of the river, only one exhibited an annual line of sight (LOS) deformation rate exceeding 50 mm/year. Two-dimensional deformation analysis indicates a strong association with terrain relief, influenced by rainfall and soil conditions. Numerical simulations of mass movement indicate a low likelihood of the landslide transitioning into rapid or full-scale failures under experimental conditions. This study provides a timely riverbank landslide evaluation workflow using InSAR and numerical modeling, which can be widely applied to other steep riverbanks in Central Asia where in-situ monitoring is insufficient.

Key words: landslide, risk evaluation, SBAS-InSAR, MassMov2D, Vakhsh River

Citation: Sun et al., 2025. Landslide Hazards Identification and Evaluation along the Vakhsh River in Tajikistan based on InSAR Time Series and the MassMov2D Model. Acta Geologica Sinica (English Edition), 99(6): 1602–1614. DOI: 10.1111/1755-6724.15350

1 Introduction

Landslides, as prevalent natural disasters, have widespread and profound impacts on human life, property safety, and the natural environment (Froude and Petley, 2018). In particular, large river systems are susceptible to landslide hazards due to their high-relief topography and intense erosion. These regions are typically characterized by significant tectonic activity, leading to the formation of steep slopes and deep valleys (Schoenbohm, 2013). As a result, they frequently experience catastrophic landslides, posing substantial threats to local communities and infrastructure. Therefore, employing targeted methods to study the formation mechanisms, movement characteristics, and prediction strategies of landslides holds significant theoretical and practical value for improving hazard prevention and mitigation efforts.

Currently, the methods for landslide monitoring are mainly divided into two categories: traditional ground-based measurements and Remote Sensing (RS) techniques. Traditional ground-based methods, such as total station measurements and Global Navigation Satellite System (GNSS) observations (Benoit et al., 2015), usually require manual field operations, which have limitations such as high costs, high risks, and restricted monitoring coverage. Although methods like terrestrial laser scanning and photogrammetry can eliminate the need for personnel to enter hazardous landslide zones for observations (Dewitte et al., 2008; Jaboyedoff et al., 2012), they still face limitations such as limited spatial coverage, dependence on favorable observation conditions, and low temporal resolution, making large-scale, high-precision continuous monitoring difficult. Since the beginning of the 21st century, optical imaging technologies utilizing high-resolution satellite and aerial imagery have been able to provide valuable information on landslide locations and displacement magnitudes. However, these methods are greatly affected by weather conditions (Mondini et al., 2019). In contrast, Interferometric Synthetic Aperture Radar (InSAR) with its high spatial resolution and all-weather, all-time capability, enables high-precision continuous monitoring of surface deformation (Tian et al., 2019; Luo et al., 2020; Huang et al., 2022). It has been successfully applied to long-term landslide monitoring and is capable of interpreting the deformation characteristics of slow-moving landslides (Colesanti et al., 2003; Tofani

* Corresponding author. E-mail: wenbin.xu@csu.edu.cn

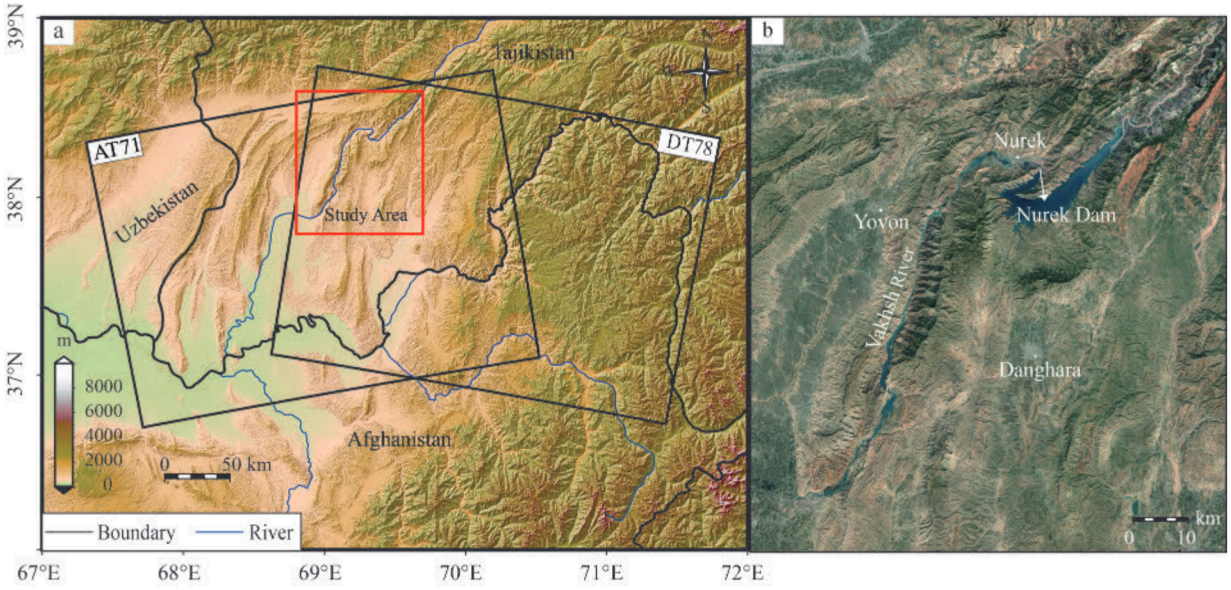

Fig. 1. Geography and topography of the study area.
The black boxes denote the footprint of Sentinel-1 orbits. The red box denotes the extent of the study area and optical background in subplot b.

et al., 2013).

Deformation monitoring can only provide the rate of landslide movement, while numerical simulation methods help to better understand the dynamic processes involved in landslide evolution (Yan et al., 2024). These methods can predict the displacement of potentially unstable slopes. Common numerical simulation approaches for landslides include the three-dimensional particle flow simulation software PFC3D based on the discrete element method (Zhang et al., 2012); the dynamic analysis method DAN3D based on an unstable flow model (Hungr and McDougall, 2009); and MassMov2D, a numerical simulation model that employs a two-dimensional finite difference method (McDougall, 2016). Compared with commonly used landslide simulation models such as PFC3D and DAN3D, MassMov2D is a novel open-source landslide modeling tool featuring strong adaptability to complex terrains, support for multiple rheological models, high computational efficiency, and a modular structure. It is capable of revealing the failure mechanisms and kinematic behaviors of landslides, making it a valuable tool for landslide research and providing scientific support for landslide hazard assessment.

The Vakhsh River is a major regional river in southern Tajikistan, located on the western margin of the Pamir orogenic belt (Fig. 1), with a length of 524 km and a drainage area of 39,100 km^2, of which 31,200 km^2 lie within Tajikistan (Sidle et al., 2024). Due to the intense ongoing tectonic deformation and frequent earthquakes in the Pamir range (Mohadjer et al., 2010; Zubovich et al., 2016), the Vakhsh River basin faces significant landslide risks. The Nurek Dam, located in the Burisangin Gorge along the middle section (Nurek River) of the Vakhsh River, is one of the highest dams in the world, with a height of approximately 300 m. The dam plays a vital role in Tajikistan's energy and irrigation infrastructure (Kosowska and Kosowski, 2022), with a design capacity of 2,700 megawatts and it supplies water to around 650,000 hectares of farmland. The region's complex geological conditions and frequent seismic activity make it particularly susceptible to geological hazards such as landslides. Previous studies have conducted preliminary investigations into the geological activity and surface deformation characteristics of the Vakhsh River Basin. In 2020, Fomenko assessed the potential for landslide-induced damming in the Vakhsh Basin and emphasized the region's active tectonics and elevated landslide risk (Fomenko et al., 2020). In 2021, Metzger used high-resolution InSAR and GNSS data to analyze crustal deformation in the Tajik Depression and its surrounding areas, revealing an eastward deformation rate of 12–24 mm/year in the Vakhsh Valley (Metzger et al., 2021). However, comprehensive monitoring and systematic risk assessments of landslides in this section of the Vakhsh River remain limited. Therefore, it is essential to monitor abnormal surface deformations and identify potential landslide hazard zones in this area, addressing a critical gap in current research.

The data processing in this study consists of three main components (Fig. 2). First, SBAS-InSAR technique was used to derive line-of-sight deformation from both ascending and descending orbit data for the Nurek section of the Vakhsh River. Second, potential landslides were identified and located by integrating the InSAR-derived deformation results with optical imagery. Finally, the landslide exhibiting the most significant deformation was selected as a representative case. The ascending and descending orbit InSAR data were then used to decompose the deformation into components parallel and normal to the slope, yielding the two-dimensional deformation information of the landslide body. Additionally, the MassMov2D numerical simulation

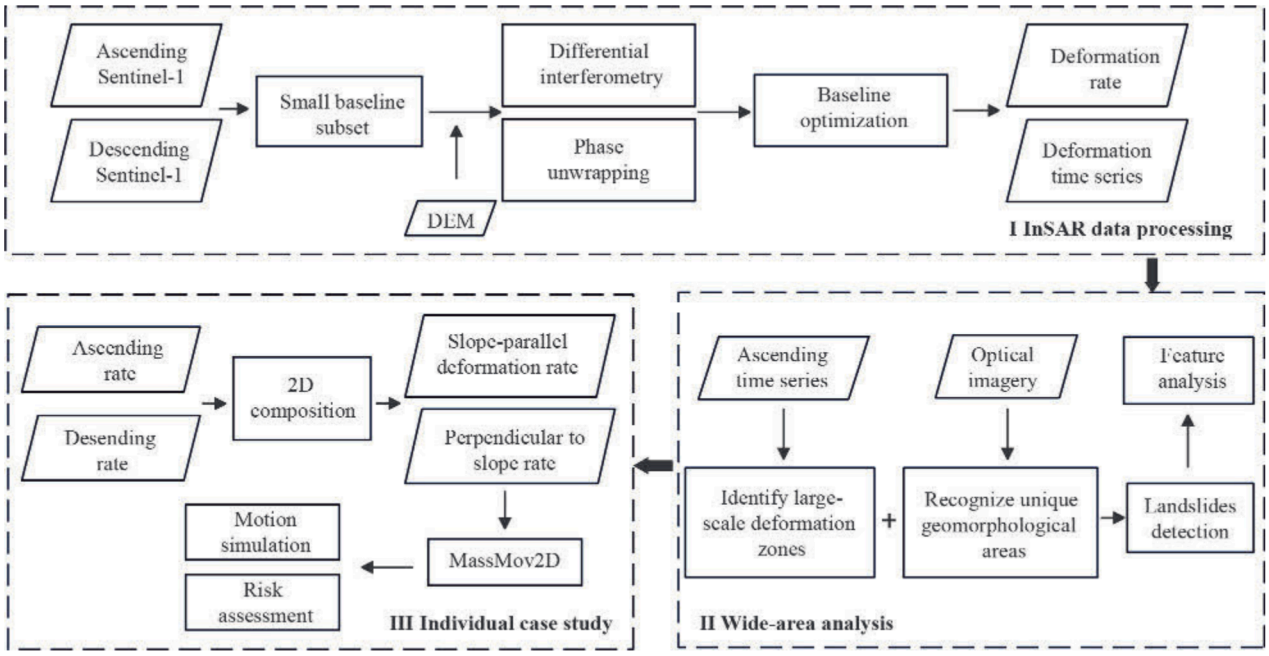

Fig. 2. Workflow of this study.

technique was employed to simulate the landslide movement process and conduct a detailed analysis of its kinematic behavior and deformation mechanisms. This study provides critical technical support for the monitoring, prediction, and management of landslide hazards in the region.

2 Data and Methodology

2.1 Data and SBAS-InSAR process

This study utilized Sentinel-1A data from the European Space Agency (ESA) in the C-band to monitor surface deformation. The Sentinel-1A satellite was launched on April 3, 2014, with a revisit time of 12 days and a stable orbit. Owing to its consistent temporal resolution and reliable imaging capabilities, it has been widely applied in surface deformation monitoring, geological hazard assessment, and urban infrastructure monitoring. In this study, a dataset of radar satellite images acquired by the Sentinel-1A mission was used to cover the southwestern region of Tajikistan from October 2017 to December 2023. The dataset comprises 182 ascending-orbit SAR images and 181 descending-orbit SAR images (Fig. 1; Table 1), providing comprehensive temporal coverage for the analysis of ground deformation in the study area. In addition to SAR data, this study also collected Shuttle Radar Topography Mission (SRTM) Digital Elevation Model (DEM) data with a spatial resolution of 90 m for the study area, to eliminate terrain-induced phase artifacts during InSAR processing (Farr et al., 2007), and to establish a geographic reference framework. Furthermore, Precise Orbit Determination (POD) was employed to minimize the influence of orbital errors on the accuracy of the deformation measurements.

In this study, SBAS-InSAR was employed to extract the ascending and descending orbit deformation fields in the study area. SBAS-InSAR was proposed in 2002 (Berardino et al., 2002). This technique utilizes a multi-master image strategy, with the basic principle of selecting SAR image pairs with short temporal and spatial baselines to generate highly coherent differential interferograms. These interferograms are then jointly solved using the Singular Value Decomposition (SVD) method to obtain deformation rates and time series within the study area. This method effectively overcame temporal and spatial decorrelation, enabling millimeter-level deformation monitoring accuracy. As such, it serves as an important tool for the early identification, dynamic monitoring, and risk assessment of landslide hazards (Zhao et al., 2019; Zhang et al., 2021).

For the ascending orbit, the image acquired on December 1, 2020, was selected as the master image, while for the descending orbit, the image from September 9, 2020, was used as the master image. The GAMMA software was utilized for data processing (Werner et al., 2000), with a multi-look factor of 20 in the range direction and 4 in the azimuth direction. During the construction of the baseline network, the temporal baseline threshold was set to one season (90 days), and the spatial baseline threshold was set to 100 m, after which interferometric pairs were generated (Fig. 3). The topographic and flat-earth phase components were removed using the SRTM DEM. The interferometric phase was then filtered using

Table 1 SAR imagery used in this study

Parameters	Ascending orbit	Descending orbit
Frame number	119	466
Path number	71	78
Acquisitions (yyyymm)	201710–202312	201710–202312
Number of images	182	181
Heading (°)	−13.3	193.3
Incidence (°)	39.5	39.5

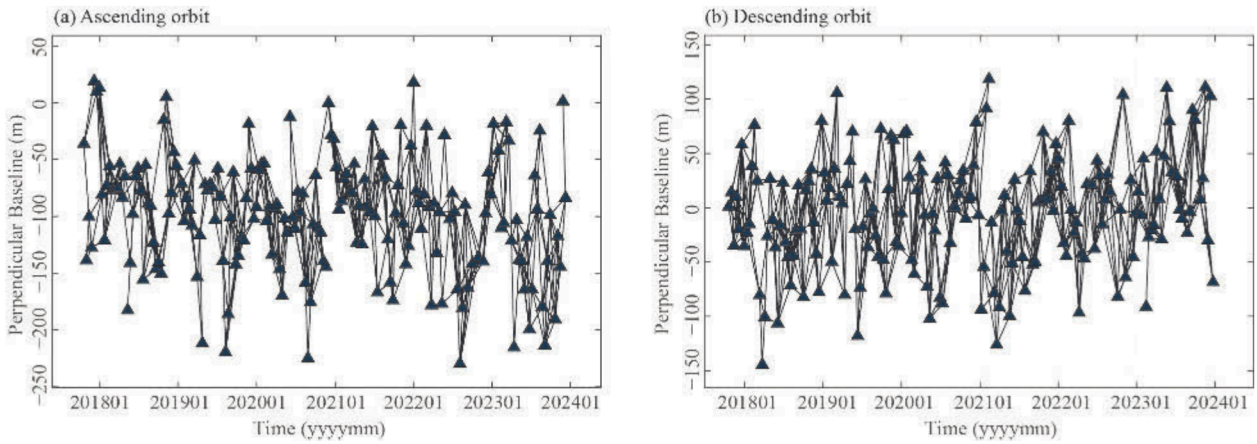

Fig. 3. Interferometric pair temporal-spatial baseline networks.
(a) Ascending orbit baseline network; (b) descending orbit baseline network.

the Goldstein filter to reduce noise effects (Goldstein and Werner, 1998). Subsequently, phase unwrapping was performed using the Minimum Cost Flow (MCF) algorithm (Chen and Zebker, 2002), with a coherence threshold of 0.2 applied during the unwrapping process to mask low-coherence areas, and the unwrapped interferograms were then filtered. Before generating the time series, baseline optimization was conducted, and individual interferograms were examined to eliminate those with significant unwrapping errors or severe decorrelation. As a result, 141 interferometric pairs were removed from the ascending track data and 89 pairs from the descending track data. Deformation time series inversion was then performed using the remaining interferometric pairs, followed by geocoding based on the DEM data.

2.2 Principle of 2D deformation decomposition

Due to the side-looking imaging geometry of Synthetic Aperture Radar (SAR), InSAR technique typically captures deformation only along the radar line of sight (LOS), referred to as LOS deformation. However, deformation usually occurs in three-dimensional space, and a single LOS measurement cannot fully represent the true surface deformation. Therefore, to more accurately and comprehensively analyze surface deformation, it is necessary to obtain deformation measurements in both the horizontal and vertical directions. Theoretically, if LOS deformation data from three different viewing geometries over the same region are available, a system of equations can be established, allowing the east–west, north–south, and vertical components of deformation to be estimated using the least squares method (Wright et al., 2004).

$$\begin{bmatrix} D_{LOS1} \\ D_{LOS2} \\ D_{LOS3} \end{bmatrix} = \begin{bmatrix} \cos\theta_1 - \sin\theta_1 \cos(\alpha_1 - \frac{3}{2}\pi) - \sin\theta_1 \sin(\alpha_1 - \frac{3}{2}\pi) \\ \cos\theta_2 - \sin\theta_2 \cos(\alpha_2 - \frac{3}{2}\pi) - \sin\theta_2 \sin(\alpha_2 - \frac{3}{2}\pi) \\ \cos\theta_3 - \sin\theta_3 \cos(\alpha_3 - \frac{3}{2}\pi) - \sin\theta_3 \sin(\alpha_3 - \frac{3}{2}\pi) \end{bmatrix} \begin{bmatrix} D_U \\ D_N \\ D_E \end{bmatrix} \quad (1)$$

where θ represents the radar wave incidence angle, α is the satellite flight azimuth angle, $\alpha - 3\pi/2$ is the angle between the projection of the LOS deformation in the horizontal direction and the north direction, D_{LOS} is the deformation observed along the radar line of sight, and D_U, D_N, D_E represent the deformation in the vertical, north–south, and east–west directions, respectively.

In practice, obtaining three independent LOS deformation components is highly challenging. Moreover, most currently orbiting SAR satellites operate in near-polar orbits with right-looking imaging modes. This observation approach causes differences in the accuracy of deformation monitoring in different directions, especially with limited sensitivity to deformation in the north–south direction (Motagh et al., 2017), resulting in weaker monitoring capability. In this study, the landslide selected for two-dimensional decomposition is located on the steep western slopes of a deeply incised, N–S-trending river valley, with the Vakhsh River situated to the east (Fig. 1). Controlled by regional geomorphology, the mountainous terrain in this area predominantly exhibits a north–south orientation, with ridges and valleys aligned accordingly, which constrains landslide movement in the north–south direction. The landslide primarily moves downslope, with displacement occurring mainly in the east–west direction, accompanied by vertical movement, while deformation in the north–south direction is minimal. As a result, the north–south deformation component is omitted in this study. The horizontal (east–west) and vertical deformations are derived from the combination of ascending and descending orbit radar observations. This approach is not only technically justified but also aligns well with the kinematic characteristics of the studied landslide.

This study mainly focuses on the deformation characteristics and patterns of landslides. Generally, landslide displacement behavior is closely related to slope gradient and slope aspect. The slope gradient represents the steepness of a surface unit, while the slope aspect is defined as the projection of the surface normal onto the horizontal plane (Fig. 4). Therefore, with the assumption that the north-south deformation component is negligible, the vertical and east-west deformation components can be further decomposed into components parallel and normal

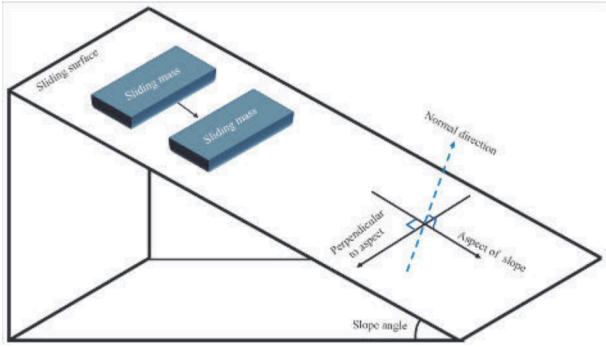

Fig. 4. The spatial relationship between the landslide direction and the normal direction.

to the landslide movement direction.

$$\begin{bmatrix} D_A \\ D_B \end{bmatrix} = \begin{bmatrix} \cos\beta - \sin\beta \\ \sin\beta - \cos\beta \end{bmatrix} \begin{bmatrix} D_E \\ D_U \end{bmatrix} \tag{2}$$

where, D_A and D_B represent the deformations along and normal to the landslide direction, respectively, β denotes the slope gradient, D_E and D_U represent the east-west and vertical deformations, respectively.

2.3 The MassMov2D model

MassMov2D is a numerical simulation technique based on the two-dimensional finite difference method, used to simulate large-scale material movements such as landslides and debris flows on complex terrain (Molinari et al., 2014). Its core principle is to describe the landslide movement process using depth-averaged fluid dynamics equations. The model treats landslide materials as a single-phase material (Savage and Hutter, 1989), whose behavior is governed by rheological properties, specifically the functional relationship between strain and stress. Furthermore, MassMov2D can accommodate various fluid flow laws, such as the Voellmy friction law and Coulomb-Bingham viscoplastic rheology, allowing it to adapt to different geological conditions and landslide types.

The core equations of the MassMov2D model consist of the conservation of mass, conservation of momentum, and rheological relationships. Equations (3) and (4) represent the momentum conservation equations, describing the balance of fluid momentum under the influences of gravity, basal friction, and turbulent viscous forces, while Equation (5) represents the mass conservation equation.

$$\frac{\partial u}{\partial t} + \cos\alpha_x u \frac{\partial u}{\partial x} + \cos\alpha_y v \frac{\partial u}{\partial y} = -\cos\alpha_x \mathrm{g} \left(\mathrm{tg}\alpha_x + k \frac{\partial(\cos\alpha_x h)}{\partial x} + \left(\frac{-u}{\sqrt{u^2+v^2}} S_f \right) \right) \tag{3}$$

$$\frac{\partial v}{\partial t} + \cos\alpha_y v \frac{\partial v}{\partial x} + \cos\alpha_x u \frac{\partial v}{\partial y} = -\cos\alpha_y \mathrm{g} \left(\mathrm{tg}\alpha_y + k \frac{\partial(\cos\alpha_y h)}{\partial y} + \left(\frac{-v}{\sqrt{u^2+v^2}} S_f \right) \right) \tag{4}$$

$$\frac{\partial h}{\partial t} + \cos\alpha_x \frac{\partial(hu)}{\partial x} + \cos\alpha_y \frac{\partial(hv)}{\partial y} = 0 \tag{5}$$

where t is the time [s]; h is the flux depth along the normal [m]; u and v are the x and y components of the velocity vector [m/s]; α_x and α_y are the angles between the sliding surface and the horizontal plane in the x and y directions [deg], respectively; g is the gravity acceleration [m/s^2]; S_f is a parameter accounting for the energy dissipation as a function of the rheological properties of the flow, assumed here to be homogeneous and constant; and k is the earth pressure coefficient: the ratio between the tangential and normal stresses.

In the MassMov2D model, different rheological models can be selected for simulation. The following equations describe the available rheological options:

$$\text{Frictional: } S_f = \tan\varphi \tag{6}$$

$$\text{Voellmy: } S_f = \tan\varphi + \frac{U^2}{h\xi} \tag{7}$$

$$\text{Bingham: } S_f = \frac{1}{h\rho}\left(\frac{3}{2}\tau_c + \frac{3\mu}{h}U\right) \tag{8}$$

$$\text{Coulomb: } S_f = \tan\varphi + \frac{1}{h\rho}\left(\frac{3}{2}\tau_c + \frac{3\mu}{h}U\right) \tag{9}$$

where, φ is the basal frictional angle; U is the velocity; ρ is the material density; τ_c is the constant yield stress; and μ is the dynamic viscosity.

The model has successfully simulated the sedimentation patterns of debris flows on the alluvial fans in the Tirol region of Austria and the French Alps (Beguería et al., 2009), showing good agreement with actual observations. Additionally, the model was used to simulate complex landslide events in the Canaria Valley, Switzerland (Molinari et al., 2012), where parameter optimization enabled the assessment of the potential for further landslide development. The flexibility and GIS integration capabilities of MassMov2D make it a crucial tool in landslide research, providing scientific support for landslide risk assessment and management.

The model requires input data such as surface topography, the initial thickness of the landslide body, and the landslide boundaries. Additional input parameters that characterize the landslide material include the Chèzy coefficient [m/s^2], the internal friction angle of the sliding mass [deg], the fluid flow velocity [m/s], and the number of simulation time steps (Molinari et al., 2012; Molinari et al., 2014; Ma et al., 2021).

3 Results

3.1 The identification and deformation in the Nurek section

The deformation rate results extracted from the ascending and descending orbit data show that the deformation rate in the region ranges from −90.9 mm/year to +13.04 mm/year for the ascending orbit, and from −49.81 mm/year to +82.79 mm/year for the descending orbit (Fig. 5). Positive values indicate deformation towards the satellite, while negative values indicate deformation away from the satellite. In most areas, the deformation rates remain relatively stable; however,

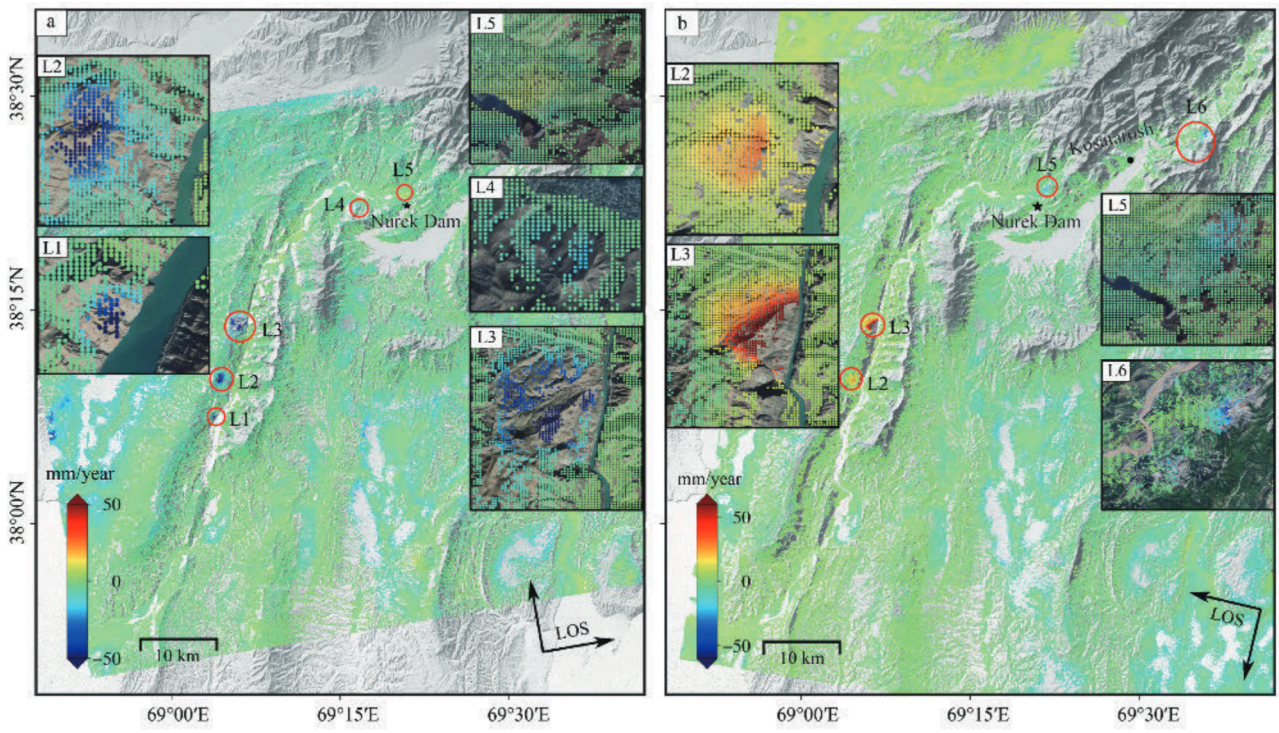

Fig. 5. The LOS displacement fields obtained using SBAS technique.
(a) Ascending orbit deformation field; (b) descending orbit deformation field. The red circles highlight the locations of detailed landslide deformation field in the inset images.

significant changes in deformation rates are observed in areas with more complex topography and urban development, where localized uplift and subsidence occur.

The deformation signals observed along the Vakhsh River exhibit notable differences between ascending and descending orbit results. By analyzing the spatial distribution characteristics of the LOS deformation rates from both orbits and integrating with optical imagery of the study area, potential landslide areas were identified. During the landslide identification process, an annual average LOS deformation rate of 10 mm/year was adopted as the threshold for identifying potential landslides (He et al., 2023), in order to ensure a more comprehensive detection of slope bodies exhibiting clear signs of activity. In the detection process, geomorphological indicators of potential landslides, such as exposed bare surfaces and steep slopes, were identified using the optical imagery of the study area. These features were then overlaid with large-magnitude and wide-coverage deformation results derived from InSAR analysis. When spatial consistency was observed between the optical features and InSAR-derived deformation anomalies, the area was classified as a potential landslide zone. Separate analyses of ascending and descending LOS deformation allowed for cross-validation of landslide locations and boundaries from different viewing geometries, enhancing the spatial accuracy and reliability of detection. The integration of InSAR deformation with optical imagery offers several advantages: (1) targeted identification of landslides along the Vakhsh River, (2) precise delineation of landslide extents, and (3) improved detection accuracy through multi-source validation.

Due to differences in imaging geometry and coherence between ascending and descending orbits, varying degrees of decorrelation occur in the LOS deformation results. As a consequence, the same landslide signal may not be simultaneously detectable in both orbit directions (Tzouvaras et al., 2020; Liang et al., 2022). Therefore, the detected landslides were named in the format of L1 (landslide 1), L2, and so forth.

In the ascending orbit deformation result, five distinct landslide signals were identified. L1, L2, and L3 are located on the left side of the river's narrow channel, with maximum deformation rates of −72.79 mm/year, −57.43 mm/year, and −90.90 mm/year, respectively. L4 is situated on a hillside near Nurek town, exhibiting a maximum deformation rate of approximately −18.73 mm/year. L5 is also located near Nurek town, close to the Nurek Dam, where the maximum landslide deformation rate is −8.04 mm/year. The region exhibited LOS movements toward the satellite, with a maximum deformation rate approaching +11.16 mm/year, which is closely related to the hydrological and geological conditions caused by the water impoundment of the Nurek Dam reservoir. In the descending orbit deformation result, four distinct landslide signals were observed. L2 and L3 are located along the Vakhsh River, with maximum deformation rates of +25.57 mm/year and +82.79 mm/year, respectively. L5, near the Nurek Dam, shows a maximum deformation rate of about −16.47 mm/year. L6 is located near Kosatarosh village in Tajikistan, with a maximum deformation rate of approximately −49.81 mm/year.

Based on the combined ascending and descending orbit deformation results, six landslide deformation signals were identified along this section of the river, with deformation mainly concentrated in areas with significant topographic variation along the riverbanks. Among these, L1, L2, and L3 are located downstream along the Vakhsh River, where the terrain is more rugged, and the river channel is narrower. These landslides exhibit relatively large deformation magnitudes and are associated with ongoing landslide activity and riverbed sedimentation. L4 and L5 are situated near Nurek town, where the deformation magnitudes are smaller but still pose certain safety risks. L6 is located in the upper reaches of the river, where a landslide could potentially lead to the formation of a dammed lake, which may subsequently alter the hydrological characteristics of the river.

3.2 The unstable rock mass of L3 landslide

L3 exhibited the largest deformation among the identified landslides in this study area and was thus selected for further analysis. By integrating deformation results from both ascending and descending orbits, the deformation rates were decomposed into east-west and vertical deformation components (Fig. 6). In the east-west deformation result, eastward movement is defined as positive, with deformation rates ranging from −5.1 mm/year to +124.1 mm/year, indicating a dominant trend of eastward displacement. In the vertical deformation result, uplift is defined as positive, with deformation rates ranging from −25.1 mm/year to +46.3 mm/year.

Furthermore, to better understand the spatial distribution characteristics of surface deformation, the east-west and vertical deformation components were projected onto directions along and normal to the slope.

Based on the magnitude of the deformation rates in these two directions and considering local topographic features, L3 was divided into three regions: R1, R2 and R3 (Fig. 7a, b). The deformation rate along the slope direction shows positive deformation in the downslope direction, with the deformation on the slope clearly exhibiting a downslope trend. In the lower part of the slope (R1), significant deformation is observed, with the maximum downslope deformation rate approaching 120 mm/year, indicating that this area may be heavily influenced by gravity. The deformation rates in the upper parts of the slope (R2 and R3) are relatively small and more stable compared to R1. The deformation rate normal to the slope shows a range from −17.38 mm/year to 70.61 mm/year. The lower part of the slope (R1), shows positive deformation, indicating local uplift and slight material accumulation. R2 and R3, on the other hand, exhibit subsidence, suggesting material loss in these areas.

We selected representative points p1, p2, and p3 in the three regions and plotted the time-series deformation curves along and normal to the slope direction for each characteristic point. The cumulative deformation along the slope direction exhibits a relatively stable linear increase, while the time-series deformation normal to the slope direction exhibits slight fluctuations, indicating that the process of material accumulation normal to the slope is more complex (Fig. 7c, d). Among all the characteristic points, p1 has the largest deformation magnitude compared to p2 and p3. The cumulative downslope deformation at p1 reaches approximately 570 mm, and the cumulative deformation normal to the slope direction is close to 250 mm. These results suggest that the region containing p1 (R1) experiences greater deformation and is less stable than the other regions.

3.3 Prediction of the potentially unstable rock mass

By integrating optical imagery, the L3 landslide, which exhibits the largest deformation magnitude along the Vakhsh River bank, was selected for further study as a potentially unstable rock mass. The MassMov2D numerical simulation technique was employed to model the landslide movement. Based on the characteristics of the landslide, the Voellmy fluid friction model was adopted for the simulation (Rickenmann and Scheidl, 2023). The potentially unstable landslide mass was delineated based on the deformation rate along the slope direction, and the average thickness of the landslide in this region was estimated to be 34 m using the "Volume–Area" power-law relationship proposed by Xu et al. (2016). In addition, for the model configuration, parameter values from previous studies (Beguería et al., 2009; Tuba, 2010; Yang et al., 2019) were referenced, the surface friction angle was set to 24°, the internal friction angle to 20°, the transition velocity from solid to fluid state of the landslide material to 15 m/s, and the total simulation duration to 100 s. Finally, the dynamic simulation and analysis of the landslide process were performed using this numerical simulation technique.

The simulation results of the sliding velocity of the unstable rock mass in the landslide indicate that the entire landslide process lasts approximately 100 s (Fig. 8). According to the simulation, at 5 s, material from the landslide source area begins to slide from the designated initiation point. By 10 s, the material rapidly accelerates downslope, reaching a velocity of nearly 40 m/s. At 20 s, the landslide area expands as additional material near the source area begins to mobilize. By 50 s, the sliding material reaches the base of the slope. At 75 s, velocity increases at the slope toe as material accumulation occurs, while the velocity near the source area begins to decrease. By 100 s, the velocity of the entire landslide body decreases to below 15 m/s and stabilizes, remaining under the specified transition velocity.

The results indicate that the initial sliding velocity is relatively high, the landslide area progressively expands, and the velocity gradually decreases until reaching a stable state. This suggests that, under the assumed conditions, once instability occurs, the landslide will develop rapidly over a short duration and eventually stabilize after a brief period.

4 Discussion

Using SBAS-InSAR technique, potential landslides along the Nurek section of the Vakhsh River were identified. InSAR monitoring results from October 2017 to December 2023 revealed several potential landslides,

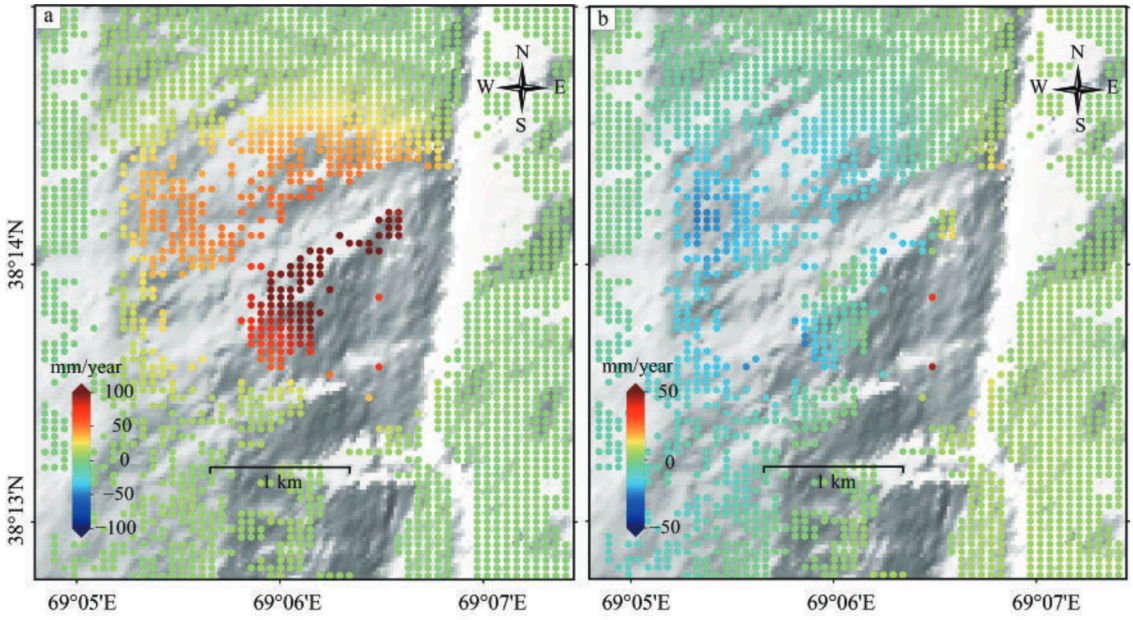

Fig. 6. The annual average two-dimensional deformation rates of L3.
(a) East–west deformation rate; (b) vertical deformation rate.

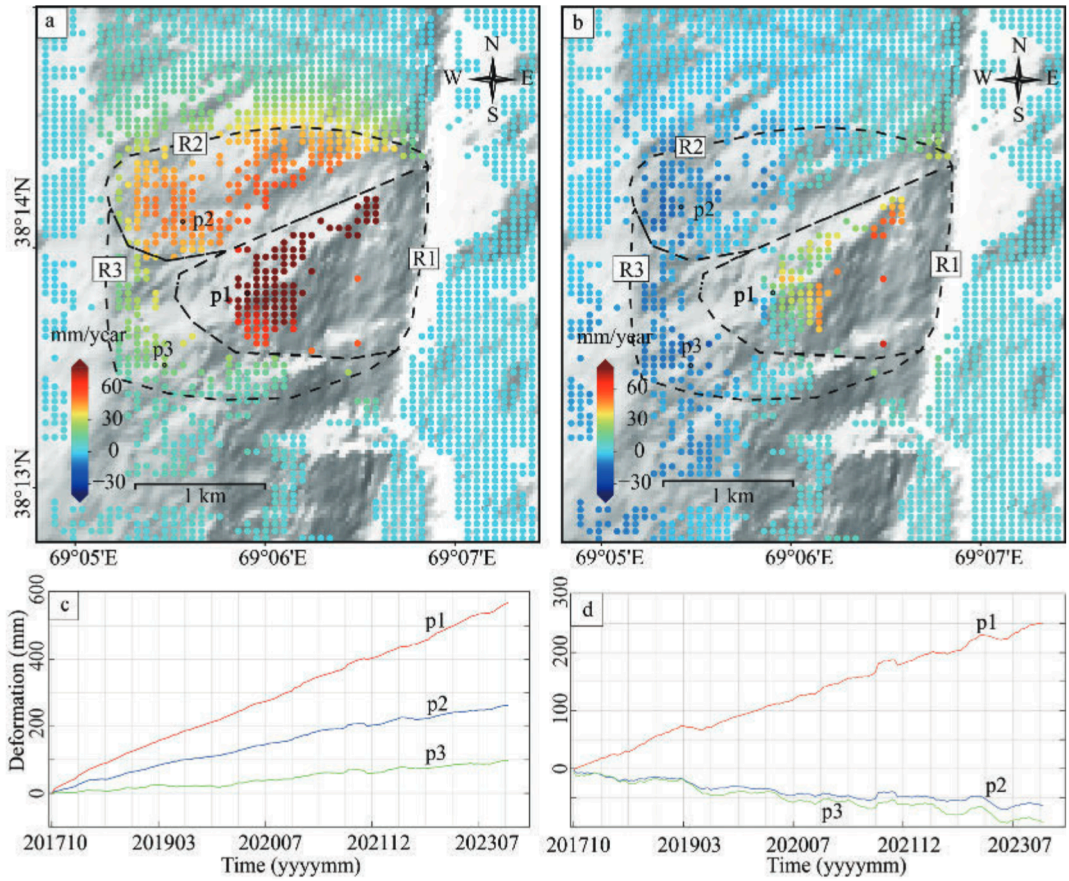

Fig. 7. The deformation rates of L3 parallel and normal to the slope direction, and the deformation time series of key points.
(a) Deformation parallel to the slope; (b) deformation normal to the slope; (c) time-series deformation curve of key points parallel to the slope; (d) time-series deformation curve of key points normal to the slope.

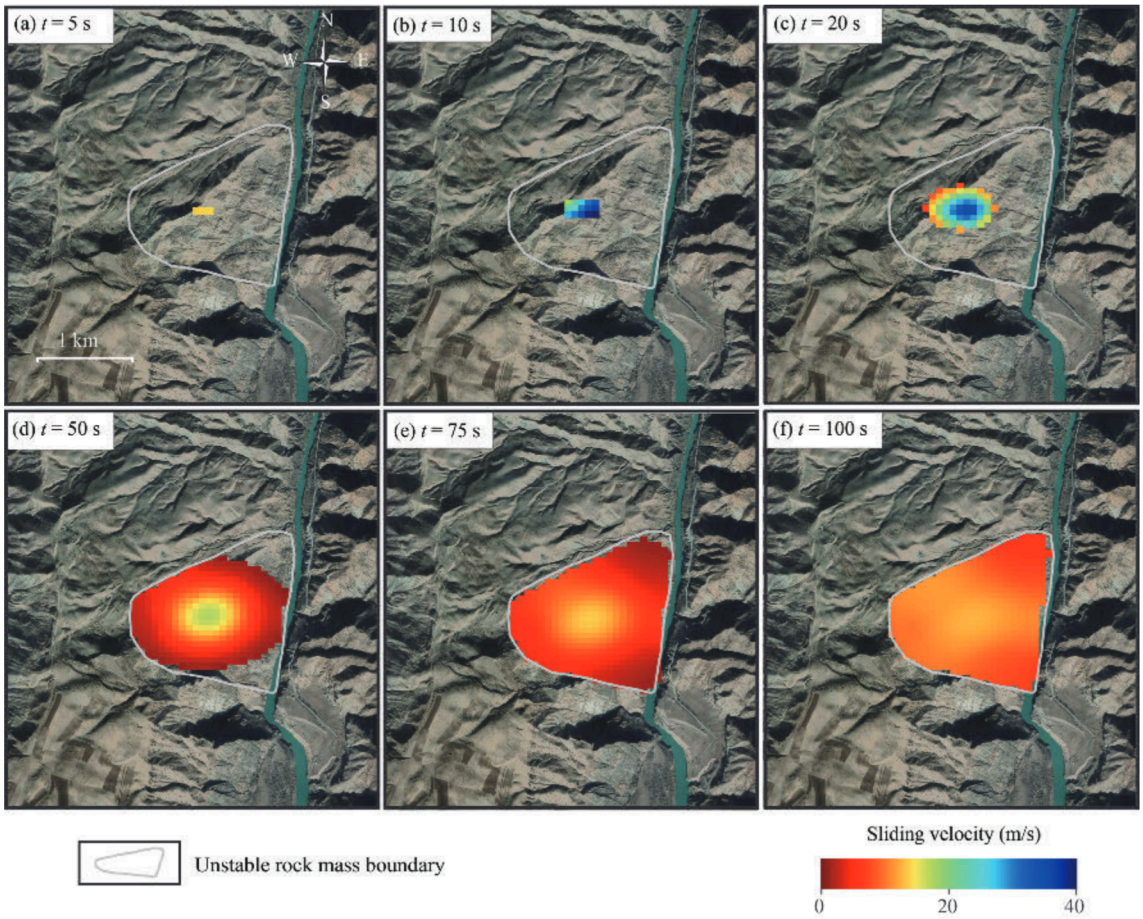

Fig. 8. Simulated sliding velocity of the unstable rock mass at (a) t =5 s, (b) t =10 s, (c) t = 20 s, (d) t = 50 s, (e) t = 75 s, and (f) t = 100 s.

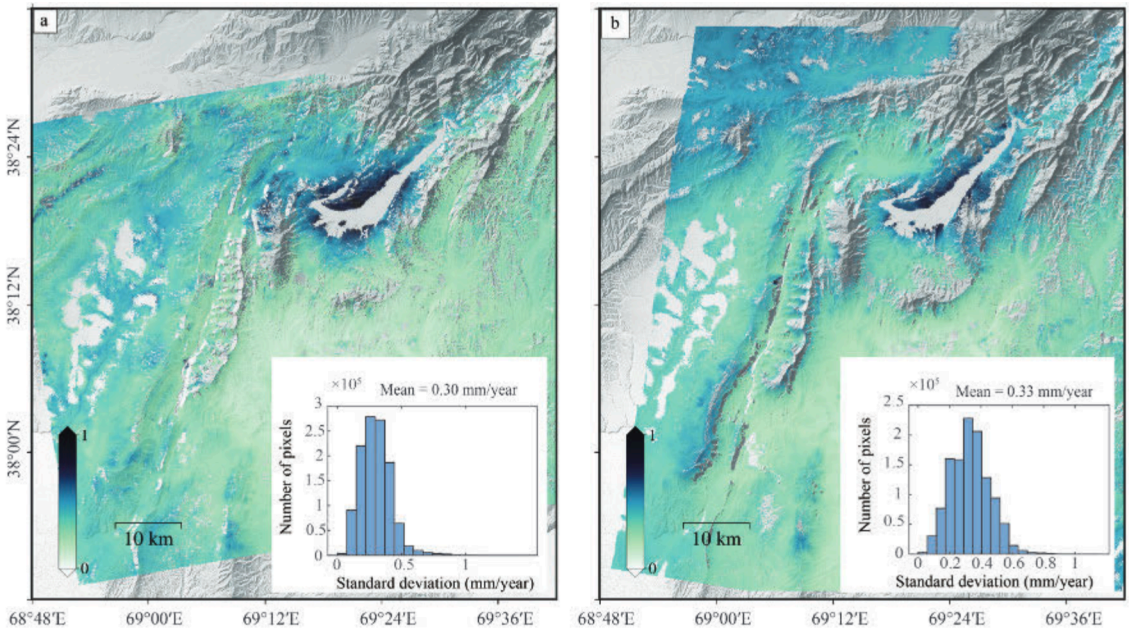

Fig. 9. Standard deviation of displacement rates derived from ascending and descending orbit deformation results.
(a) Ascending orbit; (b) descending orbit.

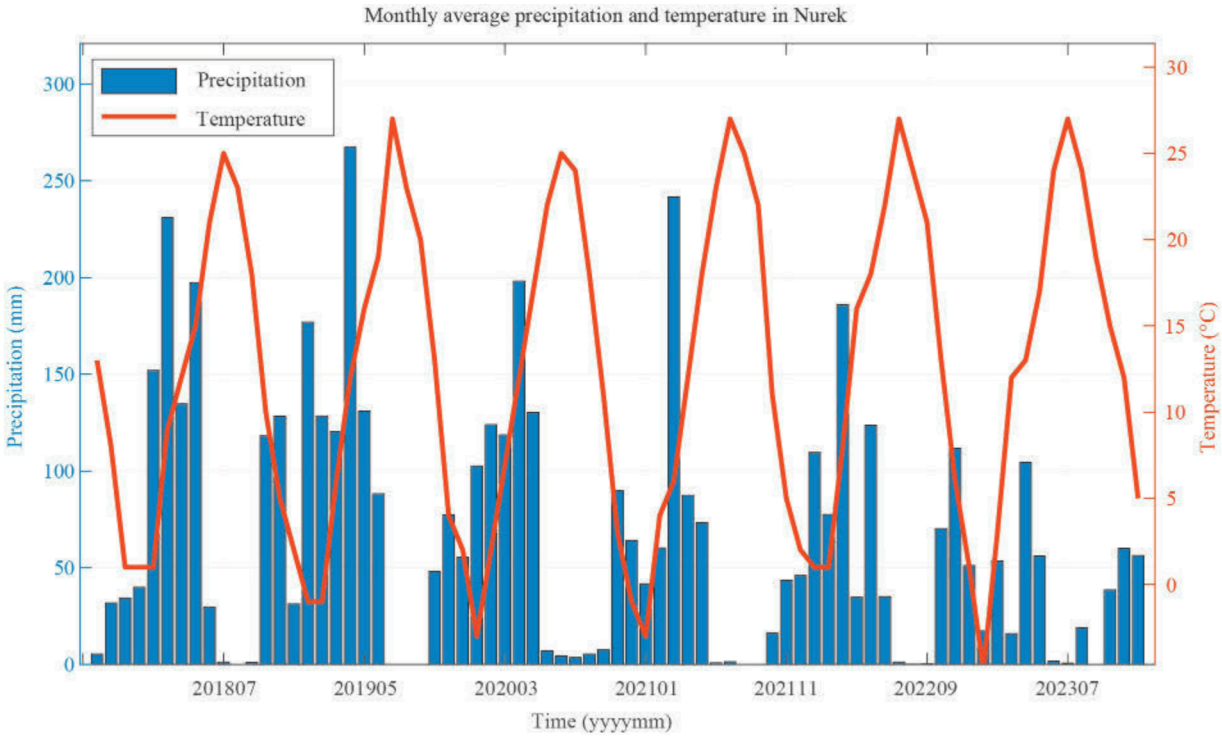

Fig. 10. Monthly average precipitation and temperature data for Nurek from October 2017 to December 2023.

with deformation signals predominantly concentrated on the western bank of the river. This indicates that landslide activity is primarily focused on that side. The likelihood of landslides is especially higher in regions with significant topographic relief (Fig. 5). However, most observed deformation rates did not exceed 50 mm/year, suggesting a relatively stable sliding trend, without evidence of severe deformation or rapid landslide events during the monitoring period.

To evaluate the accuracy of the deformation results derived from ascending and descending orbits, publicly available databases and relevant literature were reviewed. However, no GPS stations were found to be deployed within the study area, making it currently infeasible to validate the InSAR-derived deformation using GPS measurements. Therefore, this study adopts the approach proposed by Fattahi and Amelung (Fattahi and Amelung, 2015), which estimates the standard deviation of deformation rates from ascending and descending orbits as an indicator of result reliability. This method has also been applied by Liu (Liu et al., 2024) during the data processing stage of their study on active landslide classification in mountainous regions, further supporting its validity and effectiveness. The uncertainty of the velocity $\sigma^{insar}{}_{v}$ is given as:

$$\sigma_v^{insar} = \sqrt{\frac{\sum_{i=1}^{N}\left(d_i - d_i\right)}{(N-2)\sum_{i=1}^{N}\left(t_i - \bar{t}\right)^2}} \tag{10}$$

where N is the number of SAR images, d_i represents the observed range change at epoch i, and d_i denotes the predicted linear range change. t_i is the acquisition time of the SAR image at epoch i, and $\bar{t}$ is the mean acquisition time, calculated as $\bar{t} = \frac{\sum_{i=1}^{N} t_i}{N}$. The term $\sigma^{insar}{}_{v}$ represents the uncertainty caused by temporally uncorrelated residual noise in the InSAR range-change time series, relative to a selected reference pixel.

For the ascending orbit data, the proposed method yields an average standard deviation of 0.3 mm/year, while for the descending track data, the corresponding value is 0.33 mm/year (Fig. 9). These results indicate that the deformation measurements demonstrate relatively high precision.

The Nurek section is primarily composed of Paleozoic basement rocks, overlaid by Mesozoic and Cenozoic sedimentary strata. These sedimentary layers include sandstone, siltstone, mudstone, limestone, and coal seams (Sidle et al., 2024). Under steep topographic conditions, potential landslide materials experience slope-parallel deformation due to gravity, indicating that this region may serve as a landslide sliding zone or a precursor area (Shao et al., 2020). Two-dimensional deformation results show that the maximum slope-parallel deformation rate in the lower slope region, R1 (Fig.7a), is nearly 120 mm/year, with gravity identified as a primary triggering factor. Additionally, soil infiltration induced by precipitation may exacerbate slope sliding, acting as another driving factor for landslides (Han et al., 2022). Based on the region's temperature and precipitation data derived from the World Weather Online (https://www.worldweatheronline.com), the area experiences cold winters with substantial rainfall, while summers are hot and dry (Fig. 10). Frequent rain and snow events have also been reported in this region

(Sidle et al., 2024). The cyclic alternation of dry and wet conditions leads to repeated expansion and contraction of soil, which in turn compromises the structural stability of the soil (Qin et al., 2023). Moreover, seasonal changes in precipitation and sudden heavy rainfall increase soil moisture content, thereby reducing slope stability (Zhang, 2020). The region is also dominated by sierozem and sandy loam soils, which exhibit high permeability and low cohesion. These characteristics make the soils highly susceptible to erosion, thereby increasing the likelihood of landslide occurrence. In addition, soils in Tajikistan typically contain low organic matter content and show weak structural integrity (Sidle et al., 2024), further decreasing their resistance to erosion. In areas with steep slopes (slope > 30°), exposed sandy surface layers are even more vulnerable to erosion, accelerating the initiation of landslides.

We used the MassMov2D numerical simulation method to conduct an in-depth simulation and analysis of the landslide behavior of potentially unstable rock mass with significant deformation. The simulation considered factors such as sliding velocity, geological structure, and geotechnical properties. Results indicate that, under the current simulation parameters, the landslide undergoes an initial phase of rapid acceleration, followed by a gradual deceleration. The spatial extent of the landslide is limited, and no significant velocity fluctuations are observed throughout the process. These findings suggest that the deformation in the area develops gradually over the short term, and the likelihood of a sharp increase in landslide velocity is low. A comprehensive assessment of geological stability and landslide development trends further confirms that current slope activity is relatively stable, with a low probability of large-scale landslide disasters occurring in the near future. However, it is important to acknowledge that significant changes in geological or hydrological conditions could alter the landslide behavior. In the long term, while terrain and natural factors may induce localized slope failures, the overall deformation rate is expected to remain low, posing minimal immediate risk to regional safety. Therefore, continuous monitoring of landslide activity is essential, especially during periods of increased precipitation. Early detection of potential risks and timely implementation of mitigation measures are crucial for maintaining the long-term stability and safety of the region.

5 Conclusions

This study employed the SBAS-InSAR technique to identify, monitor, and assess the risk of active landslides in the Nurek segment of the Vakhsh River in southwestern Tajikistan. The results revealed six active landslides with annual average LOS deformation rates exceeding 10 mm/year. Among them, the L3 landslide exhibited the maximum deformation rate, reaching approximately 91 mm/year. Owing to the area's topographical features, landslides were predominantly concentrated on the river's left bank, where steep slopes are more prevalent, indicating a strong correlation between slope gradient and landslide occurrence. The study confirms that the slope-parallel deformation rates are highly correlated with topographical undulations. Areas with greater topographical relief are more susceptible to landslides, exhibiting larger deformation magnitudes. Additionally, rainfall and soil conditions play a significant role in influencing landslide deformation rates, particularly during wetter seasons when increased soil moisture reduces slope stability, thereby elevating landslide risks. The MassMov2D numerical simulation of unstable rockslide motion indicates that the regional landslides are relatively stable, with a low likelihood of large-scale instability in the short term. The findings highlight the effectiveness of the SBAS-InSAR technique in detecting signals of slow-moving landslides and monitoring potential landslide activities. Future research could aim to optimize numerical simulation models by incorporating more field data and multi-source remote sensing information, which would help to validate long-term deformation trends and characteristics of landslides in the region, ultimately enhancing the accuracy and reliability of landslide monitoring and risk assessment.

Acknowledgements

This research was supported by Natural Science Foundation of Hunan Province (2024JJ3031), Hunan Provincial Transportation Science and Technology Progress and Innovation Plan Project (202211), National Natural Science Foundation of China (42174023, 42304037), the Frontier Cross Research Project of Central South University (2023QYJC006), the Science and Technology Innovation Program of Fujian Province (No. 2021Y3001), the Science and Technology Innovation Program of Hunan Province (No. 2023SK2012), the Alliance of International Science Organizations (ANSO) Project (Grant No. ANSO CR PP 2022 04).

Manuscript received Feb. 20, 2025
accepted Aug. 02, 2025
guest editor: CHEN Xuanhua
edited by FEI Hongcai

References

Beguería, S., van Asch, T.W.J., Malet, J.P., and Gröndahl, S., 2009. A GIS-based numerical model for simulating the kinematics of mud and debris flows over complex terrain. Natural Hazards and Earth System Sciences, 9(6): 1897–1909.

Benoit, L., Briole, P., Martin, O., Thom, C., Malet, J.P., and Ulrich, P., 2015. Monitoring landslide displacements with the Geocube wireless network of low-cost GPS. Engineering Geology, 195: 111–121.

Berardino, P., Fornaro, G., Lanari, R., and Sansosti, E., 2002. A new algorithm for surface deformation monitoring based on small baseline differential SAR interferograms. IEEE Transactions on Geoscience and Remote Sensing, 40(11): 2375–2383.

Chen, C.W., and Zebker, H.A., 2002. Phase unwrapping for large SAR interferograms: Statistical segmentation and generalized network models. IEEE Transactions on Geoscience and Remote Sensing, 40(8): 1709–1719.

Colesanti, C., Ferretti, A., Prati, C., and Rocca, F., 2003. Monitoring landslides and tectonic motions with the permanent scatterers technique. Engineering Geology, 68(1–2): 3–14.

Dewitte, O., Jasselette, J.C., Cornet, Y., Van Den Eeckhaut, M., Collignon, A., Poesen, J., and Demoulin, A., 2008. Tracking

landslide displacements by multi-temporal DTMs: A combined aerial stereophotogrammetric and LIDAR approach in western Belgium. Engineering Geology, 99(1–2): 11–22.
Farr, T.G., Rosen, P.A., Caro, E., Crippen, R., Duren, R., Hensley, S., Kobrick, M., Paller, M., Rodriguez, E., Roth, L., Seal, D., Shaffer, S., Shimada, J., Umland, J., Werner, M., Oskin, M., Burbank, D., and Alsdorf, D., 2007. The Shuttle radar topography mission. Reviews of Geophysics, 45(2): RG2004.
Fattahi, H., and Amelung, F., 2015. InSAR bias and uncertainty due to the systematic and stochastic tropospheric delay. Journal of Geophysical Research: Solid Earth, 120(12): 8758–8773.
Fomenko, I., Strom, A., and Zerkal, O., 2020. Possibility of landslide damming in the Vakhsh River catchment and its effect on the hydraulic schemes and population. IOP Conference Series: Materials Science and Engineering, 883 (1): 012069.
Froude, M.J., and Petley, D.N., 2018. Global fatal landslide occurrence from 2004 to 2016. Natural Hazards and Earth System Sciences, 18(8): 2161–2181.
Goldstein, R.M., and Werner, C.L., 1998. Radar interferogram filtering for geophysical applications. Geophysical Research Letters, 25(21): 4035–4038.
Han Y., Wang P., Zheng Y., Yasir, M., Xu C., Nazir, S., Hossain, M.S., Ullah, S., and Khan, S., 2022. Extraction of landslide information based on object-oriented approach and cause analysis in Shuicheng, China. Remote Sensing, 14(3): 502.
He, Y., Wang, W.H., Zhang, L.F., Chen, Y.D., Chen, Y., Chen, B.S., He, X., and Zhao, Z., 2023. An identification method of potential landslide zones using InSAR data and landslide susceptibility. Geomatics, Natural Hazards and Risk, 14: 2185120.
Huang, C., Zhang, G., Zhao, D., Shan, X., Xie, C., Tu, H., Qu, C., Zhu, C., Han, N., and Chen, J., 2022. Rupture process of the 2022 Mw6.6 Menyuan, China, earthquake from joint inversion of accelerogram data and InSAR measurements. Remote Sensing, 14(20): 5104.
Hungr, O., and McDougall, S., 2009. Two numerical models for landslide dynamic analysis. Computers & Geosciences, 35(5): 978–992.
Jaboyedoff, M., Oppikofer, T., Abellán, A., Derron, M.H., Loye, A., Metzger, R., and Pedrazzini, A., 2012. Use of LIDAR in landslide investigations: A review. Natural Hazards, 61(1): 5–28.
Kosowska, K., and Kosowski, P., 2022. Energy security of hydropower producing countries: The cases of Tajikistan and Kyrgyzstan. Energies, 15(21): 7822.
Liang, J., Dong, J., Zhang, S., Zhao, C., Liu, B., Yang, L., Yan, S., and Ma, X., 2022. Discussion on InSAR identification effectivity of potential landslides and factors that influence the effectivity. Remote Sensing, 14(8): 1952.
Liu, X., Zhao, C., Yin, Y., Tomás, R., Zhang, J., Zhang, Q., Wei, Y., Wang, M., and Lopez-Sanchez, J.M., 2024. Refined InSAR method for mapping and classification of active landslides in a high mountain region: Deqin County, southern Tibet Plateau, China. Remote Sensing of Environment, 304: 114030.
Luo, X., Wang, C., Long, Y., and Yi, Z., 2020. Analysis of the decadal kinematic characteristics of the daguangbao landslide using multiplatform time series InSAR observations after the Wenchuan earthquake. Journal of Geophysical Research: Solid Earth, 125(12): e2019JB019325.
Ma, S., Xu, C., Shao, X., Xu, X., and Liu, A., 2021. A large old landslide in Sichuan Province, China: Surface displacement monitoring and potential instability assessment. Remote Sensing, 13(13): 2552.
Metzger, S., Gągała, Ł., Ratschbacher, L., Lazecký, M., Maghsoudi, Y., and Schurr, B., 2021. Tajik depression and greater Pamir neotectonics from InSAR rate maps. Journal of Geophysical Research: Solid Earth, 126(12): e2021JB022775.
Mohadjer, S., Bendick, R., Ischuk, A., Kuzikov, S., Kostuk, A., Saydullaev, U., Lodi, S., Kakar, D.M., Wasy, A., Khan, M.A., Molnar, P., Bilham, R., and Zubovich, A.V., 2010. Partitioning of India-Eurasia convergence in the Pamir–Hindu Kush from GPS measurements. Geophysical Research Letters, 37(4): L04305.
Molinari, M.E., Cannata, M., Begueria, S., and Ambrosi, C., 2012. GIS-based calibration of MassMov2D. Transactions in GIS, 16(2): 215–231.
Molinari, M.E., Cannata, M., and Meisina, C., 2014. R.massmov: An open-source landslide model for dynamic early warning systems. Natural Hazards, 70(2): 1153–1179.
Mondini, A.C., Santangelo, M., Rocchetti, M., Rossetto, E., Manconi, A., and Monserrat, O., 2019. Sentinel-1 SAR amplitude imagery for rapid landslide detection. Remote Sensing, 11(7): 760.
Motagh, M., Shamshiri, R., Haghshenas Haghighi, M., Wetzel, H.U., Akbari, B., Nahavandchi, H., Roessner, S., and Arabi, S., 2017. Quantifying groundwater exploitation induced subsidence in the Rafsanjan plain, southeastern Iran, using InSAR time-series and in situ measurements. Engineering Geology, 218: 134–151.
Qin, P.J., Liu, Y.B., Yan, Q.C., and Xuan, L.L., 2023. Effect of cycles of drying at high temperature and wetting at ambient temperature on volume change and electrical resistivity behaviors of compacted loess. Journal of Engineering Geology, 31(2): 358–367 (in Chinese with English abstract).
Rickenmann, D., and Scheidl, C., 2023. Modelling of debris-flow deposition: Terrain slope, mobility coefficient, and back-calculated basal friction coefficient. E3S Web of Conferences, 415: 07013.
Savage, S.B., and Hutter, K., 1989. The motion of a finite mass of granular material down a rough incline. Journal of Fluid Mechanics, 199: 177–215.
Schoenbohm, L., 2013. Continental-continental collision zone. Treatise on Geomorphology, 5: 13–36.
McDougall, S., 2016. 2014 Canadian geotechnical colloquium: Landslide runout analysis: Current practice and challenges. Canadian Geotechnical Journal, 54(5): 605–620.
Shao, X., Ma, S., Xu, C., Shen, L., and Lu, Y., 2020. Inventory, distribution and geometric characteristics of landslides in Baoshan City, Yunnan Province, China. Sustainability, 12(6): 2433.
Sidle, R.C., Caiserman, A., Jarihani, B., Khojazoda, Z., Kiesel, J., Kulikov, M. and Qadamov, A., 2024. Sediment sources, erosion processes, and interactions with climate dynamics in the Vakhsh River Basin, Tajikistan. Water, 16(1): 122.
Tian, Y., Jing, L.Z., Luo, Y., Li, Y., Shen, W., and Zhang, J., 2019. Monitoring subtle surface deformation due to deep dynamics using the latest InSAR technique. Acta Geologica Sinica (English Edition), 93(S1): 164.
Tofani, V., Segoni, S., Agostini, A., Catani, F. and Casagli, N., 2013. Technical Note: Use of remote sensing for landslide studies in Europe. Natural Hazards and Earth System Sciences, 13(2): 299–309.
Tuba, Z., 2010. Quantifying uncertainties in Landslide Runout Modelling (M.Sc. thesis). University of Twente, 1–80.
Tzouvaras, M., Danezis, C., and Hadjimitsis, D.G., 2020. Small scale landslide detection using Sentinel-1 interferometric SAR coherence. Remote Sensing, 12(10): 1560.
Werner, C.L., Wegmüller, U., Strozzi, T. and Wiesmann, A., 2000. Gamma SAR and interferometric processing software. ERS-ENVISAT Symposium, Gothenburg, Sweden, 16-20 Oct. 2000.
Wright, T.J., Parsons, B.E. and Lu, Z., 2004. Toward mapping surface deformation in three dimensions using InSAR. Geophysical Research Letters, 31(1): L01607.
Xu, C., Xu, X., Shen, L., Yao, Q., Tan, X., Kang, W., Ma, S., Wu, X., Cai, J., Gao, M., and Li, K., 2016. Optimized volume models of earthquake-triggered landslides. Scientific Reports, 6(1): 29797.
Yan, J., Ma, Y., Liu, L., Wang, Z., and Ren, T., 2024. Numerical simulation of rainfall-induced Xianchi Reservoir landslide in Yunyang, Chongqing, China. Acta Geologica Sinica (English Edition), 98(2): 505–517.
Yang, L., Wei, Y., Wang, W., and Zhu, S., 2019. Numerical runout modeling analysis of the loess landslide at Yining, Xinjiang, China. Water, 11(7): 1324.
Zhang, L., Dai, K., Deng, J., Ge, D., Liang, R., Li, W., and Xu, Q., 2021. Identifying potential landslides by stacking-InSAR

in southwestern China and its performance comparison with SBAS-InSAR. Remote Sensing, 13(18): 3662.
Zhang, L., Tang, H., Xiong, C., Huang, L. and Zou, Z., 2012. Movement process simulation of high-speed long-distance Jiweishan landslide with PFC 3D. Chinese Journal of Rock Mechanics and Engineering, 31: 2601–2611.
Zhang, L.M., Wang, Z.Q., Shi, L., and Kong, L., 2012. Acoustic emission characteristics of marble during failure process under different stress paths. Chinese Journal of Rock Mechanics and Engineering, 31(6): 1230–1236 (in Chinese with English abstract).
Zhang, Y., 2020. Research on the relationship between precipitation and landslide. E3S Web of Conferences, 198: 04027.
Zhao, F., Meng, X., Zhang, Y., Chen, G., Su, X., and Yue, D., 2019. Landslide susceptibility mapping of Karakorum highway combined with the application of SBAS-InSAR technology. Sensors, 19(12): 2685.
Zubovich, A., Schöne, T., Metzger, S., Mosienko, O., Mukhamediev, S., Sharshebaev, A., and Zech, C., 2016. Tectonic interaction between the Pamir and Tien Shan observed by GPS. Tectonics, 35(2): 283–292.

About the first author
SUN Yanqing, female, born in 2002 in Dazhou, Sichuan Province; Ph.D. candidate of Central South University. She is currently interested in Time series InSAR deformation monitoring and data processing. E-mail: yanqingsun0211@163.com.

About the corresponding author
XU Wenbin, male, received the Ph.D. degree in geophysics from King Abdullah University of Science and Technology, Saudi Arabia in 2015. He was a postdoc researcher with the Berkeley Earthquake Laboratory, University of California, Berkeley and an assistant professor with the Department of Land Surveying and Geo-Informatics, the Hong Kong Polytechnic University, Kowloon, Hong Kong. He is a professor and leads the Lab of Volcano and Earthquake Research in the School of Geoscience and Info-Physics, Central South University, Changsha, China. His research primarily focuses on the use of space geodesy to study ground deformation associated with a variety of geophysical and anthropogenic processes. E-mail: wenbin.xu@csu.edu.cn.